

Impact of the electron to ion mass ratio on unstable systems in particle-in-cell simulations

Q. Moreno,¹ M. E. Dieckmann,² X. Ribeyre,¹ S. Jequier,¹ V. T. Tikhonchuk,¹ and E. d'Humières¹

¹*University of Bordeaux, Centre Lasers Intenses et Applications,
CNRS, CEA, UMR 5107, F-33405 Talence, France*

²*Department of Science and Technology, Linköping University, SE-60174 Norrköping, Sweden*
(Dated: May 14, 2022)

The evolution of the Buneman and two-stream instabilities driven by a cold dilute mildly relativistic electron beam is studied as a function of the ion's charge-to-mass ratio. The growth rates of both instabilities are comparable for the selected parameters if the charge-to-mass ratio of protons is used and the Buneman instability outgrows the two-stream instability for a larger ratio. Particle-in-cell (PIC) simulations show that both instabilities grow independently during their linear growth phase. The much lower saturation amplitude of the Buneman instability implies that it saturates first even if the linear growth rates of both instabilities are equal. The electron phase space holes it drives coalesce. Their spatial size increases in time and they start interacting with the two-stream mode, which triggers the onset of electrostatic turbulence. A reduced charge-to-mass ratio results in stronger turbulence and ion heating and in an increased energy loss of the relativistic electron beam compared to that in a simulation with the correct ratio.

PACS numbers:

I. INTRODUCTION

A charge- and current neutral collision-less plasma, which is composed of two counterstreaming electron beams and ions at rest, is unstable. Such systems are frequently found in space- and astrophysical plasmas as well as in laboratory plasmas. They develop if a fast electron beam enters an initially unperturbed plasma at rest [1, 2]. The net current carried by the electron beam drives electromagnetic fields, which accelerate the electrons of the background plasma into the opposite direction. The return current of the latter eventually balances that of the beam, which restores the plasma's current-neutrality.

Several instabilities can develop after current-neutrality has been reestablished. The two-stream instability, which is driven by the interaction of both electron beams, competes with the Buneman instability or the ion acoustic instability between one electron beam and the ions if we constrain the wave vector to the direction along which the beams are drifting. The Buneman instability originally refers to the instability of one electron beam with an ion beam with the same charge density [3]. Here we use the term Buneman instability to denote a more general instability between an electron beam and an ion beam. It grows if the relative speed between electrons and ions exceeds the thermal speeds of both species significantly. The ion acoustic instability grows for lower relative speeds and at a lower exponential rate. If the direction of the wave vector is not constrained to be parallel to the beam velocity vector then the counterstreaming electron beams can drive the predominantly magnetic filamentation instability [4] or the quasi-electric oblique mode instability. Instabilities driven by relativistic electron beams are reviewed by Ref. [5].

Beam instabilities have been widely examined in the past both experimentally and theoretically. Many of

these studies were performed with particle-in-cell (PIC) simulations. The substantial computational cost of the PIC simulations implied that in some cases the development of the instabilities had to be accelerated by choosing a reduced ion mass. The reduction of the ion mass increases the exponential growth rate of the instabilities in which the ions are involved; it is the Buneman-type instability in the aforementioned case. The ion mass does, however, not affect the instabilities that develop between the counterstreaming electron beams.

A reduction of the mass of the ions in PIC simulations will thus not only speed up the instability, it will also alter the spectrum of the growing waves. The effects of a reduced ion mass on the exponential growth rate of beam instabilities have been studied systematically in Ref. [6]. It turns out that in some cases even a moderate reduction of the ion mass can have profound effects on the spectrum of the unstable waves. The process, by which the plasma is thermalized, depends in turn on the instability that saturates first. A reduction of the ion mass can, thus, alter the final state of the plasma with potentially far-reaching consequences. A plasma saturation by the filamentation instability results, for example, in strong magnetic fields [7–12], while the other instabilities drive primarily electric turbulence [13, 14]. The Buneman-type instability between the ions and the bulk electrons heats up the latter, while the two-stream instability between the counterstreaming electron beams heats up the beam electrons and possibly the bulk electrons. It is unclear how the saturation of one instability affects the other. Systematic studies are needed in order to better understand the consequences of using reduced mass ratios not only during the linear growth phase of the instabilities but also after their nonlinear saturation.

Here we test some of the results obtained in Ref. [6] with PIC simulations, which allow us to explore non-

linear effects introduced by the reduced ion mass. We limit ourselves to the mildly relativistic electron speeds, which are representative for solar energetic electrons [15–19] and for electrons that have been heated by the ablation of a solid target by a high power laser pulse [20]. Numerical artifacts, which are caused by a reduced mass ratio, become stronger with an increasing relativistic factor of the beam speed [6]. Some of our results may therefore also be relevant for numerical studies of interactions between plasma and the more energetic electron beams, which are generated by the wakefield of a laser [21, 22]. A related study involving ultrarelativistic pair beams can be found in Ref. [23]. Our parametric study is conducted in one spatial dimension and we align the beam velocity vector with the simulation direction, which suppresses the oblique mode instability and the filamentation instability. The results provided by such simulations are realistic if one electron beam is dilute and the second dense and if the beam speeds are not too high [13, 24].

Our paper is structured as follows. The linear dispersion relation of the plasma is solved and the PIC simulation method is discussed in Section 2. Section 3 presents the results of our simulation studies and they are discussed in Section 4.

II. LINEAR THEORY AND INITIAL CONDITIONS

A. Linear Theory

We consider a system composed of a relativistic electron beam with the density n_b , the reduced velocity $\beta_b = v_b/c$ and the Lorentz factor $\gamma_b = \frac{1}{\sqrt{1-\beta_b^2}}$. The beam crosses a spatially uniform plasma with the densities n_i and n_e of ions and electrons and $n_i = n_e + n_b$. The drift velocity v_e of the bulk electrons is such that it cancels out the beam current by $n_b v_b + n_e v_e = 0$. The plasma frequencies of the electrons and ions are $\omega_{pe,pi} = \sqrt{\frac{e^2 n_{e,i}}{m_{e,i} \epsilon_0}}$, where e , $m_{e,i}$, ϵ_0 are the elementary charge, the electron/ion mass and the dielectric constant, respectively. The thermal speed of a species q with the mass m_q and temperature T_q is $v_{Tq} = (k_B T_q / m_q)^{1/2}$ (k_B : Boltzmann constant). Time is normalized by ω_{pe}^{-1} , space by $c \omega_{pe}^{-1}$ and frequencies ω by ω_{pe} .

For the stability analysis, we consider the response of the system to harmonic perturbations $\propto \exp(i\mathbf{k}\cdot\mathbf{r} - \omega t)$. We reduce the system to one spatial dimension (x direction), we align the simulation direction with the beam drift velocity and define the normalized variables

$$R = \frac{m_i}{m_e}, \quad Z = \frac{k_x v_b}{\omega_{pe}}, \quad \alpha = \frac{n_b}{n_e}, \quad \Omega = \frac{\omega}{\omega_{pe}}. \quad (1)$$

We assume that the thermal speeds of both electron species are small compared to v_b and that the thermal speeds of the bulk ions and electrons are small compared

	ion mass (in m_e)	1836	400	25
$\alpha = 0.3$	maximum of δ	0.20	0.20	0.22
$\alpha = 0.03$	maximum of δ	0.10	0.10	0.21
$\alpha = 0.003$	maximum of δ	0.058	0.089	0.207

TABLE I: The growth rate of the Buneman instability for three different values of R and for α .

to v_e . The dispersion equation $K_L(Z, \Omega)$ for this cold plasma is given, for example, in Ref. [6]. Its Eigenmodes fulfill the dispersion relation $K_L(Z, \Omega) = 0$ or

$$1 - \underbrace{\frac{1 + \alpha}{R\Omega^2}}_{\text{Ion current}} - \underbrace{\frac{\alpha}{\gamma_b^3(\Omega - Z)^2}}_{\text{beam current}} - \underbrace{\frac{1}{\gamma_e^3(\Omega + \alpha Z)^2}}_{\text{return current}} = 0. \quad (2)$$

Figure 1 shows the exponential growth rate $\delta \equiv \text{Im}(\Omega)$ of the instability, which is obtained from the numerical solution of Eqn. (2), as a function of R for $\gamma_b = 2$ and for the values $\alpha = 0.3, 0.03$ and 0.003 . This instability is the superposition of the electron two-stream instability and the Buneman instability. The first one at low Z is driven by the electrons of the beam and the electronic return current. The second arises from the interaction of the electronic return current with the ions. In the limit $\alpha \ll 1$ the two-stream instability has its maximum growth rate δ at the wavenumber $Z \sim 1$, with $\delta \sim \frac{\sqrt{3}}{2^{4/3}} \frac{\alpha^{1/3}}{\gamma_b}$, and the unstable Buneman instability at the wavenumber $Z \sim 1/\alpha$, with $\delta \sim \frac{\sqrt{3}}{2^{4/3}} R^{-1/3}$.

For dense beams, the growth rate of the two-stream instability is largest regardless of R . However, when α is low, the Buneman instability may outgrow the two-stream instability for low values of R . Table I lists the maximum of the growth rate δ , localized at $Z \sim 330$, for $\alpha = 0.003$ and for three different values of R . Figure demonstrates that the choice of R affects most strongly the beam with $\alpha = 0.003$ and we focus on this case.

B. The PIC code and the initial conditions

We use the particle-in-cell (PIC) simulation code EPOCH [25]. It solves the Vlasov-Maxwell system of equations via the method of characteristics. Ampère's and Faraday's law are solved on a grid and the code fulfills Gauss's and Thomson's law to round-off precision. The plasma is approximated by an ensemble of computational particles (CPs). The momentum of each CP is updated via a discretized form of the Lorentz force equation, which uses the electromagnetic field values that have been interpolated from the numerical grid to the position of the CP. The current of each CP is interpolated back to the numerical grid and the total current, which is obtained from the summation of the current contribution of all CPs, is used to update the electromagnetic fields on the grid. We resolve one spatial dimension and the three velocity components of the CPs (1D3V).

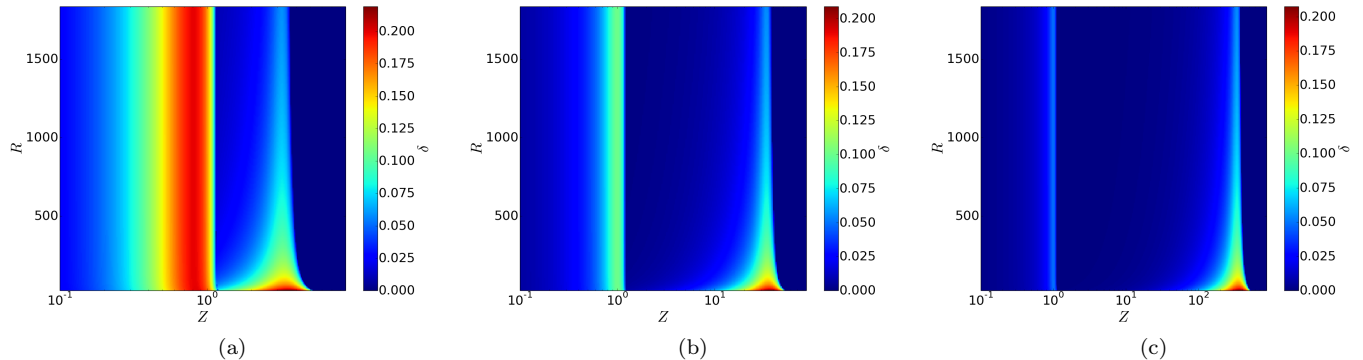


FIG. 1: Exponential growth rates $\delta(Z, R)$ obtained from the solution of the linear dispersion relation Eqn. (2) for $\gamma_b = 2$. The growth rates for $\alpha = 0.3, 0.03$ and 0.003 are shown in panel (a), panel (b), and panel (c) respectively.

The simulation domain is resolved by $N_x = 9 \times 10^4$ cells. The density of the dilute electron beam is $n_b = 0.003 n_i$ and its Lorentz factor $\gamma_b = 2$. The density of the background electrons is $n_e = 0.997 n_i$ and their mean velocity $\beta_e = 0.0026$. The length of the box is $L_x = 31.4$ and its spatial resolution is $\Delta x = 3.5 \times 10^{-4}$. Periodic boundary conditions for the electromagnetic fields and for the CPs are used. The maximum resolved wave number Z^{max} and its resolution ΔZ are respectively $Z^{max} = \beta_e \frac{\pi}{\Delta x} = 7800$ and $\Delta Z = \beta_e \frac{2\pi}{L_x} = 0.17$. The electrons and the ions have Maxwellian velocity distributions. We vary the ion mass and the temperatures of all species in a range where all beams are practically cold, so to respect the assumptions underlying Eq. 2. The temperature of the electron beam is $T_b = 10eV$, which gives the thermal speed $v_{Tb} \approx 5 \times 10^{-3} v_b$. The temperature of the bulk electrons is $T_e = 0.1eV$, which gives $v_{Te} \approx 0.2v_e$. The Debye length $\lambda_{De} = v_{Te} \omega_{pe}^{-1}$ is $\lambda_{De} = 1.25\Delta x$. We represent the ions by 250 particles per cell (ppc), the bulk electrons by 200 ppc and the beam electrons by 50 ppc.

III. SIMULATION RESULTS

A. The linear wave growth and its saturation

We compare the range of unstable wave numbers obtained from the solution of Eqn. 2 (See Fig. 1) with that of the waves in the PIC simulations and determine the saturation time as a function of R . We analyze the electric field component $E_x(x, t)$, which grows in response to the two-stream instability and Buneman instability, by performing a Fourier transform over space

$$E_x(j\Delta Z, t) = N_x^{-1} \sum_{p=1}^{N_x} E_x(p\Delta x, t) e^{-jp\Delta x \Delta Z}. \quad (3)$$

Figure 2 shows the power spectra $P_x(Z, t) = |E_x(Z, t)|^2$ for the values $R = 1836, 400$ and 25 . The wave numbers

$Z_{Bun} \sim 333$ and $Z_{TSI} \sim 1$, where the growth rates of the Buneman instability and the two-stream instability reach their maxima according to Eqn. 2, coincide with the values where the instabilities grow in Fig. 2. The instabilities start to grow after about $t \approx 15$. This delay can be attributed to the time required by the thermal noise that seeds the instabilities to grow and to the need to establish a coherent wave along the beam direction.

Figure 2 shows that both instabilities grow and saturate independently. For this low value of α the growth rate of the Buneman instability is comparable to that of the two-stream instability if $R = 1836$ and larger for smaller R . Indeed the Buneman mode at $Z \approx Z_{Bun}$ reaches about the same power as the two-stream mode at $Z \approx Z_{TSI}$ at $t \approx 100$ in Fig. 2(a) while it outgrows the two-stream modes in the cases $R = 400$ and $R = 25$.

The field power at $Z \approx Z_{TSI}$ evolves similarly in all three simulations on the displayed time interval; the evolution of this instability is unaffected by the value of R during its linear growth phase. We observe several harmonics of the wave at $Z \approx Z_{TSI}$ for $R = 1836$ and one for $R = 400$. Only a broad wave continuum is observed for $R = 25$. The peak power of the low- Z mode and the number of observed harmonics increases with R , which indicates that the wave can sustain a sine shape for a larger amplitude and for a longer time.

The waves driven by the Buneman instability are not stable. Once the wave power at Z_{Bun} has peaked the interval, in which the wave power is concentrated, is shifted in time to lower values of Z . The wave turbulence driven by the Buneman wave is amplified after $t = 250$ in the simulation with $R = 1836$. Apparently the waves couple to the two-stream mode. This coupling might be responsible for the onset of the broadband electrostatic turbulence in the cases $R = 400$ and $R = 25$.

The exponential growth rate of the Buneman instability is $\delta \sim \frac{\sqrt{3}}{24^{1/3}} R^{-1/3}$. According to this growth rate the wave amplitude will reach a given amplitude after a time $t \propto R^{1/3}$, provided that the seed electric field for the

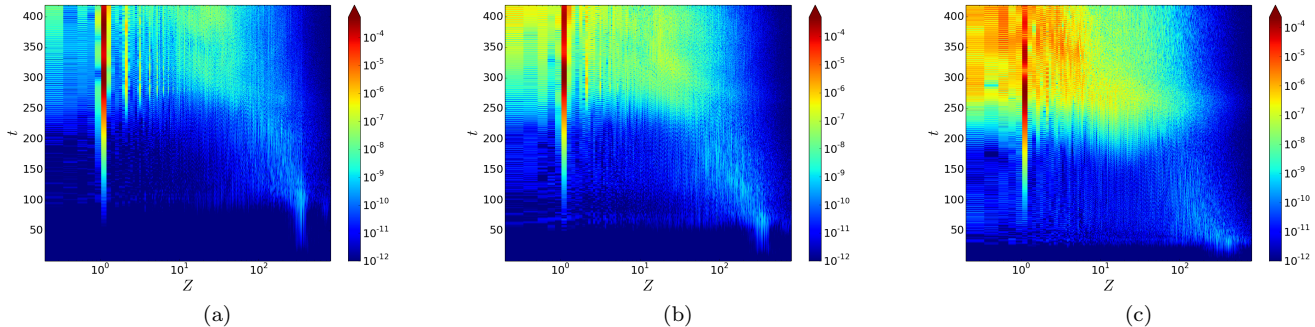


FIG. 2: The power spectrum $P_x(Z, t)$ of the electric field component E_x normalized to $m_e^2 c^2 \omega_{pe}^2 / e^2$: panel (a) corresponds to $R = 1836$, panel (b) to $R = 400$ and (c) to $R = 25$. The color scale is 10-logarithmic.

instability does not depend on R . We have performed a parametric study of the saturation time of the Buneman instability as a function of R in order to determine its scaling with the ion mass. The saturation time of the Buneman instability fulfills $t_{sat} - 15 \propto \sqrt{R}$ as shown in Figure 3. The subtracted time 15 corresponds approximately to the delay of the wave growth observed in Fig. 2. The saturation time, which is estimated with the help of the exponential growth rate, does apparently not match the observed saturation time as it is the case for the relativistic filamentation instability [26].

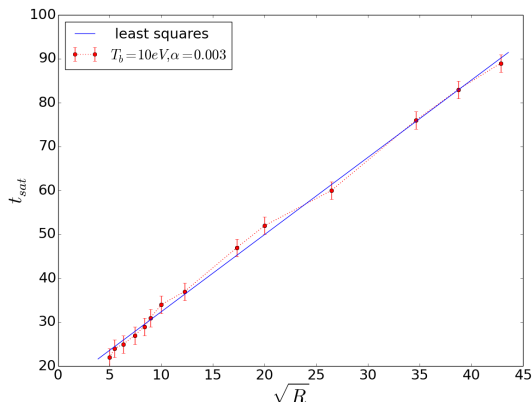


FIG. 3: Scaling of the saturation time with R . The temperature of the electron beam is $T_b = 10eV$ and the temperature of the bulk electrons is $T_e = 0.1eV$.

B. Non-linear saturation and energy transfer

We explore in this section how the value for R affects the energy exchange between the three plasma species and the electric field. We integrate for this purpose the energy density of the electric field's E_x component and the energy densities of the individual particle species over

the entire simulation box. Particle energies are measured in the reference frame, in which the total momentum vanishes at $t = 0$, which coincides with the simulation frame. We normalize all energies to the total energy.

Figure 4 shows the time evolution of all energies for the three mass ratios 1836, 400 and 25. The electric field energy grows exponentially at early times and saturates at $t \approx 90$ in Fig. 4(a), at $t = 50$ in Fig. 4(b) and at $t \approx 25$ in Fig. 4(c). The faster rise of the field energy at low R reflects the larger growth rate of the Buneman instability. The field energies at the time the Buneman instability saturates are the same in all simulations, which suggests that it is caused by the interaction between the wave and electrons. This is confirmed by Fig. 4. The energy the ions gain when the Buneman instability saturates does increase with decreasing R but it remains small compared to the energy gain of the bulk electrons. The energies of the electric field, the ions and the bulk electrons all increase in Fig. 4 when the Buneman instability saturates. Energy conservation implies that the saturation of the Buneman instability must have extracted energy from the beam electrons. The electric field energy decreases after the saturation of the Buneman instability and this energy decrease depends on R .

The electric field energy rises again after $t = 200$. Its growth rate is the same in all three simulations as expected for the two-stream instability. The electric field energy saturates at $t \approx 300$ and reaches a peak value that is about 20% of the beam electron energy for $R = 1836$ and 400. The two-stream instability saturates earlier and at a lower peak value for $R = 25$. The phase speed of the wave, which is driven by the two-stream instability, does not depend on R . This wave will enforce a stronger reaction of ions with a low value of R . We have observed this stronger reaction already in Fig. 2(c), which revealed a lower peak power of the electric field and strong broadband turbulence that set in when the wave saturated. Figure 4 also shows that the bulk electron energy closely follows that of the electric field until its saturation, after which the individual energies evolve differently in the three simulations.

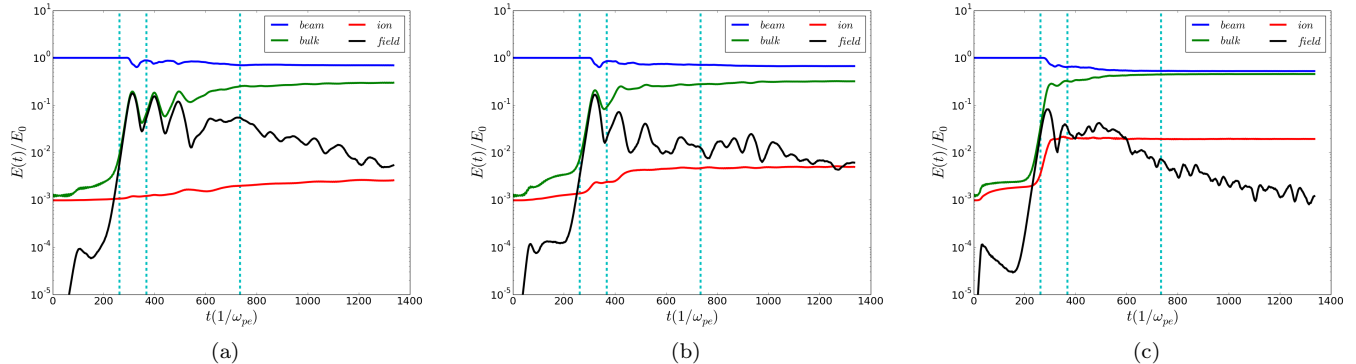


FIG. 4: Panel (a) shows the particle and field energies for a mass ratio $R = 1836$, panel (b) for a mass ratio 400 and panel (c) for the mass ratio 25. The temperature of the electron beam is $T_b = 10\text{eV}$ and the temperature of the bulk electrons is $T_e = 0.1\text{eV}$, the dashed lines correspond to the times $t = 262, 367$ and 734 .

The energies of the electric field and of the bulk electrons oscillate in phase three times for $R = 1836$. The beam electron energy oscillates in antiphase. The ion energy hardly reacts to these oscillations for $R = 1836$. The ions with $R = 400$ are accelerated by the electric field, which damps the energy oscillations of the electrons and the electric field. A reduction of the ion mass to $R = 25$ boosts their response to the electric field and the damping of the oscillations of the energies of the electrons and the electric field. The energies of the bulk electrons and of the beam electrons seem to converge in all simulations and they become almost equal for $R = 25$. However, the mean energy per electron is still much larger for the beam particles since $\alpha \ll 1$. At the simulations's end, the ion energy in the simulation with $R = 25$ exceeds that in the simulation with $R = 1836$ by an order of magnitude.

The simulations, which provided the data shown in Fig. 3, were followed over a longer time in order to determine the efficiency of the energy transfer from the electron beam to the bulk electrons as a function of R . Figure 5 shows their results. The bulk electrons gain between 25% and 30% of the total energy after the two-stream instability's saturation if $R > 100$. The energy increases from 30% to almost 50% for decreasing values $R < 100$. A reduction of R thus enhances the transfer of energy from the electron beam to the bulk electrons. This effect is, however, only observed if the electron beam is cold. Increasing the temperature of the electron beam from 10 eV to 5 keV suppresses the rise of the final energy of the bulk electrons at low values of R .

C. Phase space density distributions

We compare in this section the phase space density distributions of the particle species at the times $t = 262, 367$ and 734 , which are marked by the vertical dashed lines in Fig. 4. Figure 6 shows the distributions for the run with

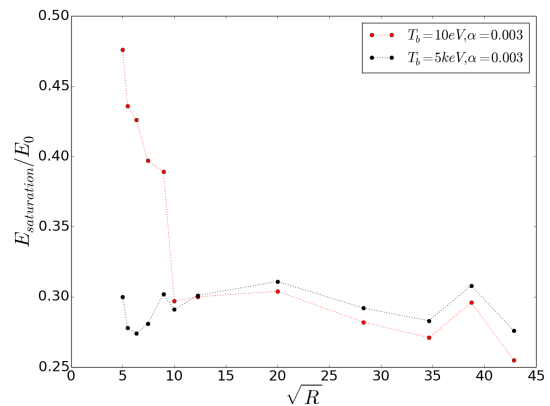


FIG. 5: The saturation energy of the bulk electrons at $t = 1250$ in units of the total energy for $\alpha = 0.003$ and for the temperature $T_b = 10\text{eV}$ for the electron beam. The temperature of the bulk electrons is $T_e = 0.1\text{eV}$

$R = 1836$. The dilute electron beam drives resonantly a Langmuir wave with a positive phase speed ω/k slightly below the beam speed. This wave is still growing at the time $t = 262$. Its phase is most easily determined from the phase space density distribution of the bulk electrons in Fig. 6(d), which shows sinusoidal oscillations of the mean speed with x . The bulk velocity is zero at $x \approx 0.3$ and $x \approx 5.7$ and the electrostatic potential must thus have an extremum at these positions. The surrounding electrons are attracted towards these points and the potential is thus positive. The beam electrons in Fig. 6(a) gyrate around the maxima of the positive potential and some are trapped by it. The different response of both electron species is caused by a phase speed of the wave, which is much larger in the reference frame of the bulk electrons than in that of the beam electrons.

The number density of the beam electrons at the cusps

$$m_i = 1836 m_e$$

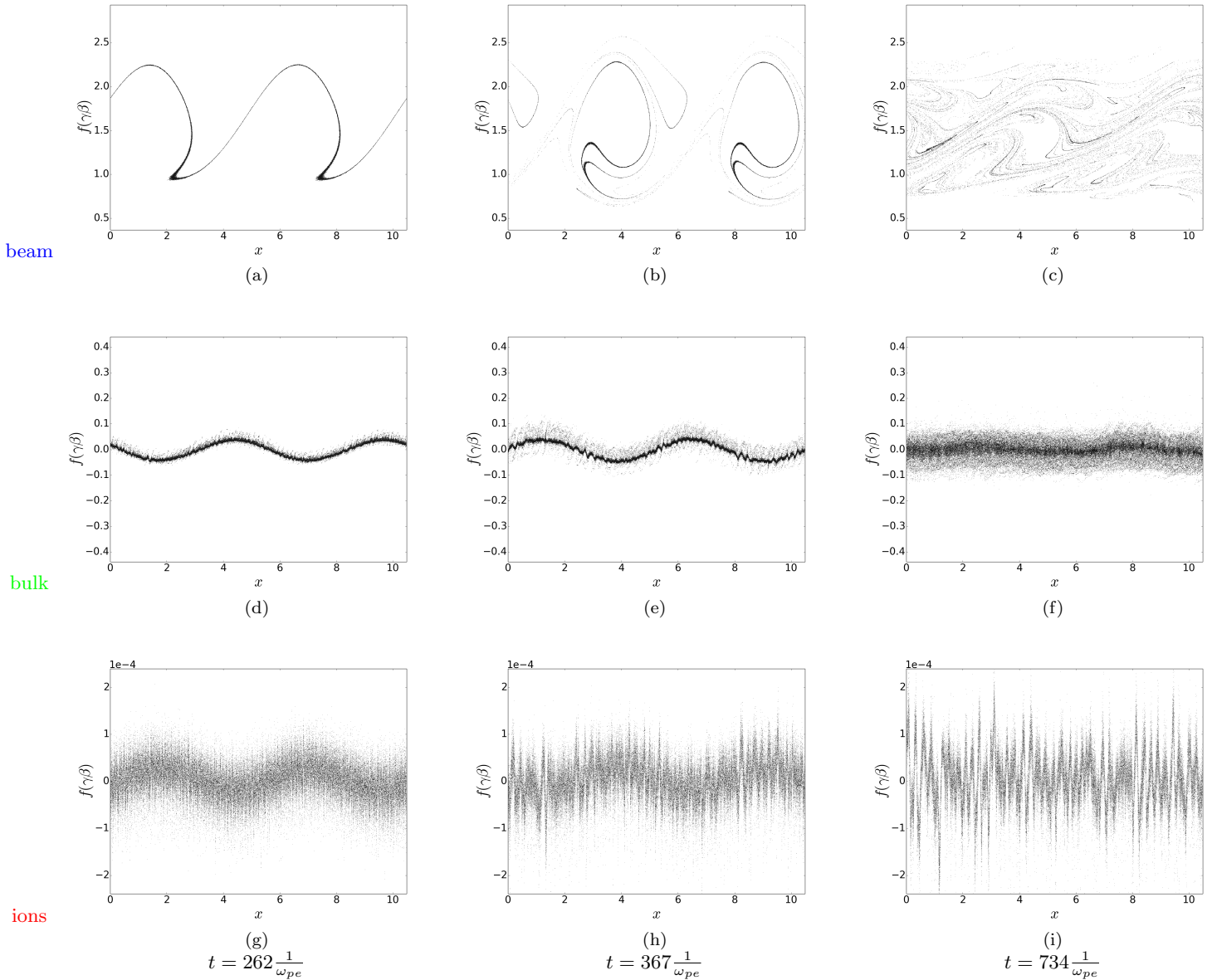


FIG. 6: The particle phase space density distributions. The first row shows the distribution of the beam electrons, the second row that of the bulk electrons and the bottom row that of the ions. The first column shows the distributions at the time $t = 262$, the second at the time $t = 367$ and the third one at the time $t = 734$. The ion mass is $m_i = 1836m_e$ and the initial temperatures of the beam and bulk electrons are $T_b = 10eV$ and $T_e = 0.1eV$.

at $x = 2$ and $x = 7.4$ is large and their momentum $\beta\gamma \approx 1$ is below the initial beam momentum, which explains why the beam energy in Fig. 4(a) has been reduced at this time. The distribution of the beam electrons is changing into the phase space vortices or phase space holes, which form when an electrostatic instability with a wave vector that is aligned with the beam velocity [27, 28] saturates. The ions oscillate in the wave's electric field at an amplitude that is small due to the large value of R .

The bulk electrons in Fig. 6(d) show oscillations with

a short wave length. These are electron phase space holes that were driven by the Buneman instability. The time, during which a phase space hole develops, is comparable to the bouncing frequency of a particle with the charge q and mass m in a wave potential $\omega_b = (qkE/m)^{1/2}$, where kE is the product of wavenumber and electric field amplitude (See Ref. [14] and references cited therein). Electron phase space holes form 5 times faster than ion phase space holes even for the lowest ion mass $R = 25$. Electron phase space holes are thus responsible for

the initial saturation of the Buneman instability in all simulations, which explains why it always saturated at about the same electric field amplitude.

The electron phase space holes have been driven by a resonance of the ion beam with the Langmuir wave and their propagation speed in the rest frame of the bulk electrons is close to that of the ions. In its rest frame, an electron phase space hole is associated with an electrostatic potential that is almost static and it can thus easily accelerate the ions. The speed gain of the ions with $R = 1836$ remains small due to the short acceleration time and we observe only small oscillations of the ion velocity at small wavelengths in Fig. 6(g).

The Langmuir wave, which grew in response to the two-stream instability, has propagated towards increasing x and both cusps in the electron beam distribution have rotated further at the time $t = 367$. The mean momentum of the cusp electrons in Fig. 6(b) has increased compared to that in Fig. 6(a), which explains why the beam energy in Fig. 4(a) has increased. This cusp and the current, which is associated with its motion, is causing the periodic exchange of energy between the beam electrons on one hand and the bulk electrons and the electric field on the other hand. The beam distribution in Fig. 6(b) reveals the presence of multiple beams. The bouncing in the sinusoidal potential of the electrostatic wave disperses the electrons, which results in a reduction of the amplitude of the energy oscillations.

The electron phase space holes, which were driven by the Buneman instability, coalesce to larger ones [27]. The larger phase space holes in the bulk electrons in Fig. 6(e) yield now noticeable short-wavelength oscillations in the ion distribution displayed by Fig. 6(h); the latter are ion acoustic waves. Coalescence explains why the characteristic wave number of the waves, which were generated by the Buneman instability, decreases in time in Fig. 2.

The growing ion acoustic waves and the growth of the amplitude of the velocity oscillations of the phase space holes in the bulk electrons hints at an instability between both species that is still active long after the Buneman instability saturated. The velocity oscillations of the bulk electrons caused by the two-stream instability have a wave length that is large compared to that of the ion acoustic waves in Fig. 6(h) and an amplitude that is larger than the electron thermal speed in Fig. 6(e). The therefrom resulting drift between the bulk electrons and ions is thus large and it could destabilize the ion acoustic waves and heat the bulk electrons. The driving mechanism of the small-scale perturbations could thus be similar to that of the oscillating two-stream instability [29] if the laser-generated electrostatic beat wave were replaced by the two-stream mode.

The ion oscillations have increased their amplitude at $t = 734$ and the density of the hot component of the bulk electrons has increased. The long-wavelength oscillation of the bulk distributions has vanished, which implies that the beam-driven Langmuir wave has been damped out. The beam electrons have been dispersed and form now a

turbulent distribution with a wide velocity spread in Fig. 6(c). The velocity spread is comparable to the velocity width of the electron phase space holes at the earlier time, which is in turn determined by the velocity interval $v_{tr} = (2qE/mk)^{1/2}$ around the wave's phase velocity where a particle gets trapped by the wave. The beam distribution is well-separated from the bulk electron distribution along the velocity direction.

Figure 7 shows the phase space density distributions obtained from the run with $R = 25$ at the same times as the ones discussed in Fig. 6. The electron beam distribution in Fig. 7(a) shows that a large phase space hole is about to form. Its shape is practically identical to that in the run with $R = 1836$, confirming that the two-stream instability is not affected by the value of R . The earlier development of the Buneman instability and the faster onset of the ion acceleration have rendered the bulk plasma in Figs. 7(d,g) significantly more turbulent than that in Figs. 6(d,g). A comparison of Fig. 7(h) with Fig. 6(h) reveals a population of energetic ions for the case $R = 25$ that was not present in the simulation with $R = 1836$.

The waves driven by the Buneman instability and the electron phase space holes they drive have a negative phase speed in the simulation frame. Ions, which are accelerated in the propagation direction of the electron phase space hole, stay in phase with its electric field for a longer time and are thus accelerated to a larger speed modulus. The larger charge-to-mass ratio of ions with $R = 25$ meant that they could be accelerated to a larger speed than those with $R = 1836$. The ions were accelerated at the expense of the electric field energy. The ion acceleration is thus probably responsible for the damping of the Buneman instability-driven waves between $t = 262$ and $t = 367$ in Fig. 4(c).

The electric field, which is associated with the turbulent bulk plasma, covers a broad range of wave numbers that extends even to Z_{TSI} (See Fig. 2(c)). Both bulk distributions still show modulations with a long wavelength, which sustain the wave that grows in response to the two-stream instability. Figure 4(c) shows that the electric field energy decreases after $t = 262$, while the energies of the ions and the bulk electrons grow to values well above the ones in the simulations with $R = 1836$ and 400. The growth of the energy of the bulk species slows down at $t = 367$ and the electric field energy remains high and constant until $t \approx 600$. Figure 7(b) shows that an electron phase space hole is still present in the electron beam distribution, but it does no longer have the quasi-circular shape as the one in Fig. 6(b). Figures 7(e, h) demonstrate that the energy gain of both bulk plasma species is due to a temperature increase and not due to a spatial modulation of the mean speed as in the simulation with $R = 1836$.

The temperature increase of the bulk plasma results in an increase of its thermal pressure. The increasing thermal pressure reduces the density modulation in response to the electric field of the wave. The reduced

$$m_i = 25 m_e$$

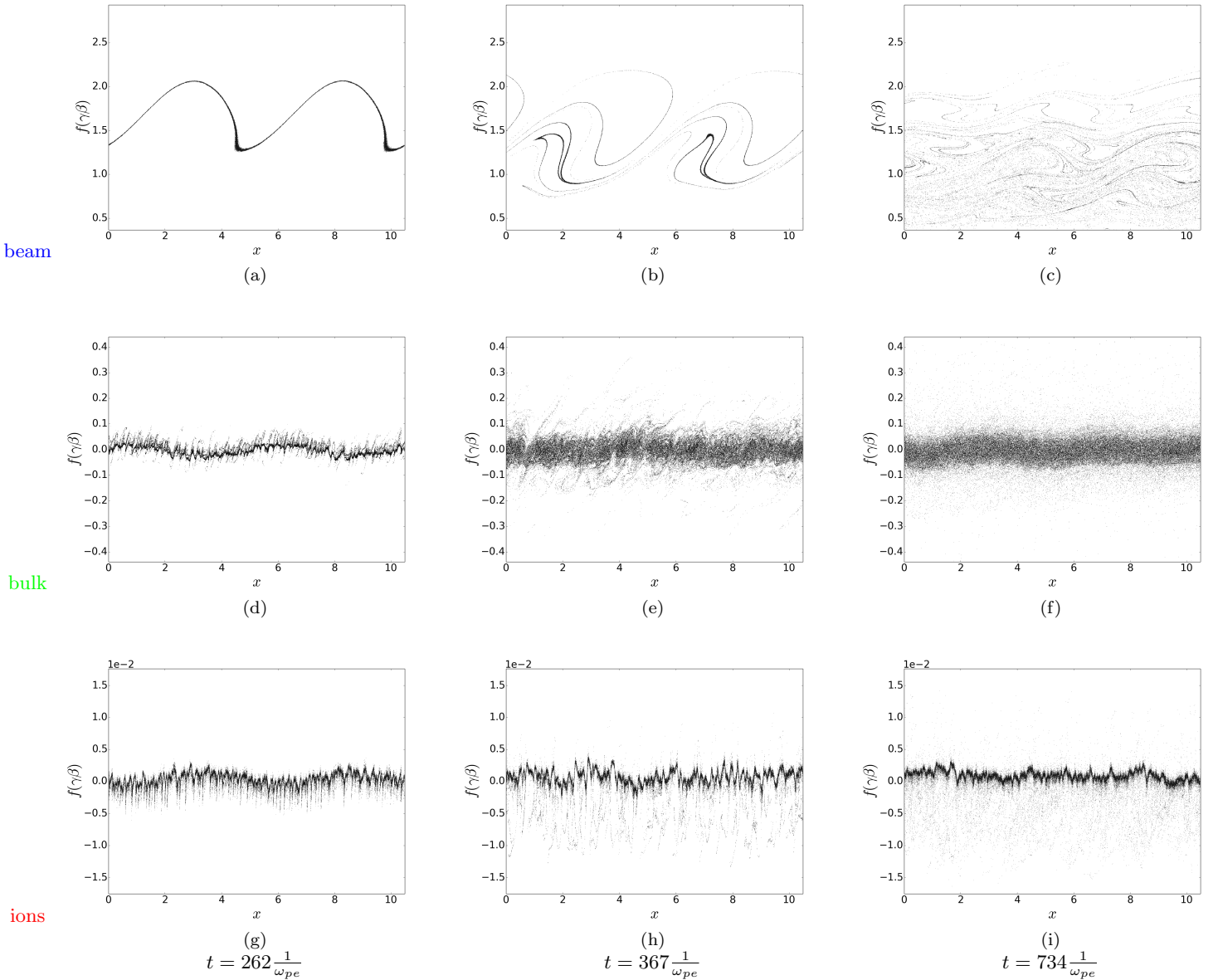


FIG. 7: The particle phase space density distributions. The first row shows the distribution of the beam electrons, the second row that of the bulk electrons and the bottom row that of the ions. The first column shows the distributions at the time $t = 262$, the second at the time $t = 367$ and the third one at the time $t = 734$. The ion mass is $m_i = 25m_e$ and the initial temperatures of the beam and bulk electrons are $T_b = 10eV$ and $T_e = 0.1eV$.

density modulation causes in turn a reduction of its electric field amplitude and of the spatial modulation of the mean velocity of the bulk electrons and ions. The electron phase space hole does no longer interact with the bulk plasma via the electrostatic wave and hence we do no longer observe oscillations due to a periodic energy exchange between the particles and the electric field.

The ion distribution in Fig. 7(h) shows elongated tails that extend to a speed -10^{-2} . These tails form during the nonlinear evolution of the Buneman instability.

Even though the density of these tails is low, they carry a significant momentum. The mean momentum of the ions has become negative, which is initially compensated for by a momentum increase of the bulk electrons. The momentum change of the bulk electrons results in a net current, which drives an electric field that interacts in turn with the ions and with the electron beam. The effect of this electric field can be seen from Fig. 7(c). The electron beam distribution is as diffuse as that in Fig. 6(c) and its velocity width is comparable. The mean ve-

locity of the beam is, however, lower by a value 0.3 for all x . The simultaneous reduction of the velocity of all beam electrons can only be accomplished by an electric field that is spatially almost uniform. The lost kinetic energy is transferred to the bulk plasma. This process has been discussed previously in Ref. [1].

IV. DISCUSSION

We have studied here the interplay of the Buneman instability with the two-stream instability by solving the linear dispersion relation and by means of particle-in-cell simulations. Our motivation was to test some of the results obtained in Ref. [6], which examined the interplay of all instabilities driven by a cold relativistic electron beam that propagates through an unmagnetized background plasma. The dominant mode was determined in Ref. [6] as a function of the beam density and relativistic factor based on its linear growth rate.

We considered only wave vectors that were parallel to the beam velocity vector, which excluded the Weibel instability and the oblique modes, and allowed us to perform the simulations at a reasonable computational cost. We have considered the case of a mildly relativistic dilute electron beam, for which the growth rates of electrostatic instabilities are comparable to or larger than those of the electromagnetic filamentation instability [2]. Such beams are formed by the solar energetic electrons that propagate through the solar wind and we find such beams in laser-plasma experiments.

The initial conditions for the instabilities were selected such that the Buneman instability would grow as fast as the two-stream instability for the charge-to-mass ratio of protons and faster for a larger ratio. This case study can thus serve as a testbed for whether or not the plasma evolution is indeed determined by the first instability that saturates. Our results are as follows.

We found that the scaling of the exponential growth rate of the Buneman instability can not be used to estimate its saturation time like it can be done in the case of the electromagnetic instabilities [30]. The electrostatic instabilities did not start to grow immediately after the simulation commenced. The saturation time counted from the time the instabilities started to grow was estimated from a series of PIC simulations and we found that it scaled like $R^{-1/2}$ rather than $R^{-1/3}$. The latter scaling

is suggested by the solution of the linear dispersion relation. The deviation is likely to be related to the faster acceleration of ions with a large charge-to-mass ratio by the waves driven by the Buneman instability. Indeed only the bulk electrons gained energy when the Buneman instability saturated in the case of a low charge-to-mass ratio while ions also gained energy when the charge-to-mass ratio was high. Despite similar growth rates the two-stream instability saturated long after the Buneman instability because the wave could grow to a much larger amplitude before it saturated by means of particle trapping. The main effect an increased ion charge-to-mass ratio had on the evolution of the two-stream instability was to damp the periodic exchange of energy between the electron beam and the bulk electrons.

The saturation of the Buneman instability did initially not affect the growth of the two-stream instability and the ion's charge-to-mass ratio had thus initially no effect on the two-stream instability. Hence the evolution of the plasma is not always determined by the instability that saturates first. The coalescence of the electron phase space holes, which were driven by the Buneman instability, implied that the characteristic wavelength of their electric field became comparable to that of the two-stream instability, which resulted in an amplification of the small-scale turbulence that was strong for a large charge-to-mass ratio of the ions. The mechanism that amplified the small-scale turbulence resembled that of the oscillating two-stream instability, in which an electrostatic wave with a long wavelength couples to electrostatic waves with a shorter wavelength. The turbulence grew at the expense of the beam's kinetic energy and the beam was slowed down much more in the case of the light ions than in the case of the protons.

V. ACKNOWLEDGMENTS

This work was supported by the French National Research Agency Grant ANR-14-CE33-0019 MACH. This work was also granted access to the HPC resources of CINES and TGCC under allocations A0020510052 and A0030506129 made by GENCI (Grand Equipement National de Calcul Intensif), and has been partially supported by the 2015-2019 grant of the Institut Universitaire de France obtained by CELIA.

-
- [1] R. V. Lovelace, and R. N. Sudan, *Phys. Rev. Lett.* **27**, 1256 (1971).
 - [2] L. E. Thode, and R. N. Sudan, *Phys. Fluids* **18**, 1564 (1975).
 - [3] O. Buneman, *Phys. Rev. Lett.* **1**, 8 (1958).
 - [4] F. Califano, R. Prandi, F. Pegoraro, and S. V. Bulanov, *Phys. Rev. E* **58**, 7837 (1998).
 - [5] A. Bret, L. Gremillet, and M. E. Dieckmann, *Phys. Plasmas* **17**, 120501 (2010).
 - [6] A. Bret, and M. E. Dieckmann, *Phys. Plasmas* **17**, 032109 (2010).
 - [7] Y. Kazimura, J. I. Sakai, T. Neubert, and S. V. Bulanov, *Astrophys. J.* **498**, L 183 (1998).
 - [8] M. Honda, J. Meyer-ter-Vehn, and A. Pukhov, *Phys. Plasmas* **7**, 1302 (2000).
 - [9] L. O. Silva, R. A. Fonseca, J. W. Tonge, J. M. Dawson,

- W. B. Mori, and M. V. Medvedev, *Astrophys. J.* **596**, L121 (2003).
- [10] J. I. Sakai, R. Schlickeiser, and P. K. Shukla, *Phys. Lett. A* **330**, 384
- [11] C. H. Jaroschek, H. Lesch, and R. A. Treumann, *Astrophys. J.* **618**, 822 (2005).
- [12] K. I. Nishikawa, J. Niemiec, P. E. Hardee, M. Medvedev, H. Sol, Y. Mizuno, B. Zhang, M. Pohl, M. Oka, and D. H. Hartmann, *Astrophys. J.* **698**, L10 (2009).
- [13] L. E. Thode, and R. N Sudan, *Phys. Rev. Lett.* **30**, 732 (1973).
- [14] M. E. Dieckmann, P. Ljung, A. Ynnerman, and K. G. McClements, *Phys. Plasmas* **7**, 5171 (2000).
- [15] L. Muschietti, *Solar Phys.* **130**, 201 (1990).
- [16] E. P. Kontar, *Astron. Astrophys.* **375**, 629 (2001).
- [17] K. L. Klein, S. Krucker, G. Trottet, and S. Hoang, *Astron. Astrophys.* **431**, 1047 (2005).
- [18] H. A. S. Reid, and E. P. Kontar, *Astrophys. J.* **721**, 864 (2010).
- [19] H. A. S. Reid, and H. Ratcliffe, *Res. Astron. Astrophys.* **14**, 773 (2014).
- [20] M. Tabak et al. *Phys. Plasma* **1**, 1629 (1994).
- [21] E. Esarey, C. B. Schroeder, and W. P. Leemans, *Rev. Mod. Phys.* **81**, 1229 (2009).
- [22] J. Warwick, T. Dzelzainis, M. E. Dieckmann, W. Schu-
maker, D. Doria, L. Romagnani, K. Poder, J. M. Cole,
A. Alejo, M. Yeung, K. Krushelnick, S. P. D. Mangles,
Z. Najmudin, B. Reville, G. M. Samarina, D. D. Symes,
A. G. R. Thomas, M. Borghesi, and G. Sarri, *Phys. Rev.
Lett.* **119**, 185002 (2017).
- [23] L. Sironi, and D. Giannios, *Astrophys. J.* **787**, 49 (2014).
- [24] M. Tzoufras, C. Ren, F. S. Tsung, J. W. Tonge, W. B. Mori, M. Fiore, R. A. Fonseca, and L. O. Silva, *Phys. Rev. Lett.* **96**, 105002 (2006).
- [25] T. D. Arber, K. Bennett, C. S. Brady, A. Lawrence-Douglas, M. G. Ramsay, N. J. Sircombe, P. Gillies, R. G. Evans, H. Schmitz, A. R. Bell, and C. P. Ridgers, *Plasma Phys. Contr. Fusion* **57**, 113001 (2015).
- [26] A. Bret, A. Stockem, R. Narayan, and L. O. Silva, *Phys. Plasmas* **21**, 072301 (2014).
- [27] K. V. Roberts, and H. L. Berk, *Phys. Rev. Lett.* **19**, 297 (1967).
- [28] T. M. O'Neil, J. H. Winfrey, and J. H. Malmberg, *Phys. Fluids* **14**, 1204 (1971).
- [29] D. N. Gupta, K. P. Singh, A. K. Sharma, and N. K. Jaiman, *Phys. Plasmas* **11**, 5250 (2004).
- [30] A. Bret, A. Stockem, F. Fiuza, C. Ruyer, L. Gremillet, R. Narayan, and L. O. Silva, *Phys. Plasmas* **20**, 042102 (2013).